GEOPHYSICS, VOL. 57, NO. 10 (NOVEMBER 1992), P. 1409–1418, 8 FIGS.

Topographic responses in magnetometric resistivity modeling

Chieh-Hou Yang* and Hung-Wen Tseng‡

ABSTRACT

The magnetometric resistivity (MMR) topographic responses due to earth topography were simulated using a finite-element method. An algorithm was developed and the computer program was verified by comparison with analytic responses for half-space and contact models. The topographic responses for different rugged surfaces were computed, and the model results indicate topographic effects can affect MMR sounding interpretation. In general, MMR topographic responses do depend on surface form; the more rugged the ground surface is, the larger the MMR topographic anomaly will be. These topographic effects will decrease as the distance between the source (and/or receiver) position and the high relief area is increased. We only address the problem of determining MMR anomalies over a two-dimensional (2-D) topography. A numerical example illustrates an effective means of reducing the terrain effects for a 45-degree dipping fault model incorporating a 45-degree ramp surface, suggesting that the finite-element modeling technique does provide a means of determining topographic correction for MMR sounding data.

INTRODUCTION

The electrical resistivity responses from a geoelectric sounding survey conducted on a rugged surface are affected not only by the subsurface structure but also by ground surface relief. The topographic anomaly will contaminate the field data which is usually used to infer the geoelectric depth section. Therefore, a reliable interpretation cannot be obtained from the resistivity data unless the topographic correction has been done. Topographic corrections for both two- and three-dimensional (2- and 3-D) electrical resistivity problems have been studied by Fox et al. (1980) and Holcombe and Jiracek (1984). The methods suggested by these authors provide a way to reduce a great deal of topographic noise in electric surveys.

Rather than measuring the potential field by the dc resistivity method, the magnetometric resistivity (MMR) method measures the magnetic field produced by the noninductive current flowing from grounded current electrodes. Based on the similarity between the two geoelectric methods, we have to evaluate the topographic effect on the MMR sounding. Until now the only available model study on the terrain effect in MMR surveys was demonstrated by Oppliger (1984) by using the surface integral equation method.

In this paper, a 2-D modeling of topographic effects for the MMR survey is studied using the finite-element method instead of a finite-difference approach (Pai and Edwards, 1983; Tseng et al., 1985). The results provide the user of the MMR method with a guide of what to expect in some simple field situations. These results are also complimentary to those presented by Oppliger (1984). Although, 2-D modeling is useful only under certain circumstances, we hope the modeling technique described may extend its application to estimating and removing 3-D effects in MMR surveys. In the modeling process, a nonhomogeneous element is used to calculate the MMR topographic anomaly. The accuracy of the numerical solutions is examined by comparing them with analytical solutions, and results show that the rugged topography can produce significant effect on the MMR measurements.

THEORETICAL DEVELOPMENT

Basic equations for electric potential

In a steady state, the current density $\mathbf{J}$ in an isotropic medium is related to the electric field by Ohm's law:

$$\mathbf{J} = \sigma\mathbf{E}, \tag{1}$$

where σ, the electrical conductivity, is a function of position (x, y, z). The conservation of charge for a point source of the current I_s has the form

Presented at the 59th Annual International Meeting, Society of Exploration Geophysicists. Manuscript received by the Editor June 20, 1990; revised manuscript received January 14, 1992.
*Institute of Geophysics, National Central University, Chungli, Taiwan 32054, Republic of China.
‡Dept. of Material Sciences and Mineral Engineering, University of California at Berkeley, Berkeley, CA 94720.

$$-\nabla \cdot [\sigma(x, y, z)\nabla\phi(x, y, z)] = I_s\delta(x)\delta(y)\delta(z), \quad (2)$$

where ϕ is the electric potential. If we assume the electric potential is zero at infinities ($y = +\infty$ and $y = -\infty$), then the functional $F(\phi(x, y, z))$ in the domain (x, λ, z) can be evaluated using variational formulation and a Fourier cosine transformation (e.g. Coggon, 1971)

$$F(\tilde{\phi}(x, \lambda, z)) = \int\int_A \sigma\left[\left(\frac{\partial\tilde{\phi}}{\partial x}\right)^2 + \left(\frac{\partial\tilde{\phi}}{\partial z}\right)^2\right]dx\,dz + \lambda^2\int\int_A \sigma\tilde{\phi}^2\,dx\,dz - 2\int\int_A \tilde{\phi}I_s\delta(x_s)\delta(z_s)\,dx\,dz - \int_s \tilde{\phi}\sigma\nabla\tilde{\phi}\cdot ds \quad (3)$$

As the conductivity within the geoelectric structure is known, then the electric potential distribution made by a point current source on the earth's surface can be obtained under the condition that the functional $F(\tilde{\phi})$ is a minimum. The mixed boundary condition suggested by Dey and Morrison (1979) is used to solve this potential distribution.

Basic equations for magnetic field

The equations used to compute the MMR responses are derived from the Biot-Savart law and Ohm's law (Edwards et al., 1978):

$$\mathbf{B}(x, y, z) = \frac{\mu}{4\pi} \times \int_{V'} \frac{\nabla'\phi(x', y', z') \times \nabla'\sigma(x', y', z')}{\sqrt{[(x-x')^2 + (y-y')^2 + (z-z')^2]}}\,dx'\,dy'\,dz', \quad (4)$$

where

μ is the magnetic permeability and assumed to be the same as that of free space;
σ is the electric conductivity;
ϕ is the electric potential;
$\mathbf{B}$ is the magnetic field intensity;
(x, y, z) is the point at the ground surface;
(x', y', z') is the point within the half-space ($z' > 0$); and
V' is the volume for the whole half-space.

Assume that σ is a function of x' and z' only, then, $\partial\sigma(x', y', z')/\partial y' = 0$. Through the Fourier cosine transformation, equation (4) becomes

$$\mathbf{B}(x, y, z) = \frac{\mu}{4\pi} \times \int_{V'} \frac{\mathbf{i}\dfrac{\partial\sigma}{\partial z'}\dfrac{\partial\phi}{\partial y'} + \mathbf{j}\left(\dfrac{\partial\sigma}{\partial x'}\dfrac{\partial\phi}{\partial z'} - \dfrac{\partial\sigma}{\partial z'}\dfrac{\partial\phi}{\partial x'}\right) - \mathbf{k}\dfrac{\partial\sigma}{\partial x'}\dfrac{\partial\phi}{\partial y'}}{\sqrt{[(x-x')^2 + (y-y')^2 + (z-z')^2]}}dx'\,dy'\,dz'$$

$$= -\mathbf{i}\frac{2}{\pi}\int_0^\infty \lambda\sin(\lambda y)\left[\frac{\mu}{2\pi}\int_{A'}\frac{\partial\sigma}{\partial z'}\tilde{\phi}(x', \lambda, z') \times K_0(\lambda\sqrt{(x-x')^2 + (z-z')^2})\,dx'\,dz'\right]d\lambda + \mathbf{j}\frac{2}{\pi}\int_0^\infty \cos(\lambda y)\left[\frac{\mu}{2\pi}\int_{A'}\left(\frac{\partial\sigma}{\partial x'}\frac{\partial\tilde{\phi}}{\partial z'} - \frac{\partial\sigma}{\partial z'}\frac{\partial\tilde{\phi}}{\partial x'}\right) \times K_0(\lambda\sqrt{(x-x')^2 + (z-z')^2})\,dx'\,dz'\right]d\lambda + \mathbf{k}\frac{2}{\pi}\int_0^\infty \lambda\sin(\lambda y)\left[\frac{\mu}{2\pi}\int_{A'}\frac{\partial\sigma}{\partial x'}\tilde{\phi}(x', \lambda, z') \times K_0(\lambda\sqrt{(x-x')^2 + (z-z')^2})\,dx'\,dz'\right]d\lambda, \quad (5)$$

where

K_0 is the modified Bessel function of order zero;
λ is the spatial wave number; and
A' is the cross-sectional area on the $x' - z'$ plane for the whole half-space.

Hence, the component of magnetic field $\mathbf{B}(x, y, z)$ can be calculated from an inverse Fourier cosine transform of $\mathbf{B}(x, \lambda, z)$, the bracketed terms in equation (5), provided that $\tilde{\phi}(x', \lambda, z')$ is known.

NUMERICAL SIMULATION

The technique of finite-element method

The well established finite-element technique is used for this study by dividing the subsurface into numerous triangular finite elements. The unknown potential values $\tilde{\phi}_m$ within each element can then be interpolated from known potential values at the three corners. The coordinates of the element vertices and related electric properties, such as the electric conductivity $\tilde{\phi}_m^{(e)}$, can be interpolated in the same way. Figure 1a illustrates the finite-element mesh in which i and k represent the indices of nodes in the x- and z-directions, respectively. The indices $i = 1, M$ and $k = 1, N$ correspond to the boundary surfaces at $x = -\infty$ to $+\infty$ and $z = 0$ to $+\infty$, respectively. For instance, at a trianguler element (see Figure 1b) (x_1, z_1), (x_2, z_2), and (x_3, z_3) are the coordinates of the vertices of the element and $\tilde{\phi}_1^{(e)}$, $\tilde{\phi}_2^{(e)}$, and $\tilde{\phi}_3^{(e)}$ are the associated potential at the three vertices, respectively.

The computation of electric potential

The electric potential and conductivity at a certain point in the triangular element can be derived through an interpolation function of the following form:

$$\tilde{\phi}_m^{(e)}(x, \lambda, z) = N_1^{(e)}\tilde{\phi}_1^{(e)} + N_2^{(e)}\tilde{\phi}_2^{(e)} + N_3^{(e)}\tilde{\phi}_3^{(e)} \quad (6)$$

$$\sigma_m^{(e)}(x, z) = N_1^{(e)}\sigma_1^{(e)} + N_2^{(e)}\sigma_2^{(e)} + N_3^{(e)}\sigma_3^{(e)} \quad (7)$$

and

$$\underline{\tilde{\Phi}}^{(3)} = \begin{bmatrix} \tilde{\Phi}_1^{(e)} \\ \tilde{\Phi}_2^{(e)} \\ \tilde{\Phi}_3^{(e)} \end{bmatrix} \quad \underline{\sigma}^{(e)} = \begin{bmatrix} \sigma_1^{(e)} \\ \sigma_2^{(e)} \\ \sigma_3^{(e)} \end{bmatrix} \quad \underline{N}^{(e)} = \begin{bmatrix} N_1^{(e)} \\ N_2^{(e)} \\ N_3^{(e)} \end{bmatrix}, \tag{8}$$

where

$$\begin{aligned} N_1 &= (a_1 + b_1 x + c_1 z)/2A \\ N_2 &= (a_2 + b_2 x + c_2 z)/2A \\ N_3 &= (a_3 + b_3 x + c_3 z)/2A \end{aligned} \tag{9}$$

and

$$\begin{cases} a_1 = x_2 z_3 - x_3 z_2 \\ b_1 = z_2 - z_3 \\ c_1 = x_3 - x_2 \end{cases} \quad \begin{cases} a_2 = x_3 z_1 - x_1 z_3 \\ b_2 = z_3 - z_1 \\ c_2 = x_1 - x_3 \end{cases}$$

$$\begin{cases} a_3 = x_1 z_2 - x_2 z_1 \\ b_3 = z_1 - z_2 \\ c_3 = x_2 - x_1 \end{cases} . \tag{10}$$

In equation (9), A is the element area. Substituting equations (6) and (7) into equation (3) and minimizing the function $F(\tilde{\Phi}^{(e)})$, we can get the element equation as follows:

$$\left\{ \frac{\sigma_1^{(e)} + \sigma_2^{(e)} + \sigma_3^{(e)}}{12A_m} \begin{bmatrix} b_1^2 + c_1^2 & b_1 b_2 + c_1 c_2 & b_1 b_3 + c_1 c_3 \\ b_1 b_2 + c_1 c_2 & b_2^2 + c_2^2 & b_2 b_3 + c_2 c_3 \\ b_1 b_3 + c_1 c_3 & b_2 b_3 + c_2 c_3 & b_3^2 + c_3^2 \end{bmatrix} \right.$$

$$\left. + \frac{A_m \lambda^2}{60} \begin{bmatrix} 6\sigma_1^{(e)} + 2\sigma_2^{(e)} + 2\sigma_3^{(e)} & 2\sigma_1^{(e)} + 2\sigma_2^{(e)} + \sigma_3^{(e)} & 2\sigma_1^{(e)} + \sigma_2^{(e)} + 2\sigma_3^{(e)} \\ 2\sigma_1^{(e)} + 2\sigma_2^{(e)} + \sigma_3^{(e)} & 2\sigma_1^{(e)} + 6\sigma_2^{(e)} + 2\sigma_3^{(e)} & \sigma_1^{(e)} + 2\sigma_2^{(e)} + 2\sigma_3^{(e)} \\ 2\sigma_1^{(e)} + \sigma_2^{(e)} + 2\sigma_3^{(e)} & \sigma_1^{(e)} + 2\sigma_2^{(e)} + 2\sigma_3^{(e)} & 2\sigma_1^{(e)} + 2\sigma_2^{(e)} + 6\sigma_3^{(e)} \end{bmatrix} \right\} \underline{\tilde{\Phi}}^{(e)} = I_s \delta(x_s)\delta(z_s) \begin{bmatrix} N_1^{(e)} \\ N_2^{(e)} \\ N_3^{(e)} \end{bmatrix} \tag{11}$$

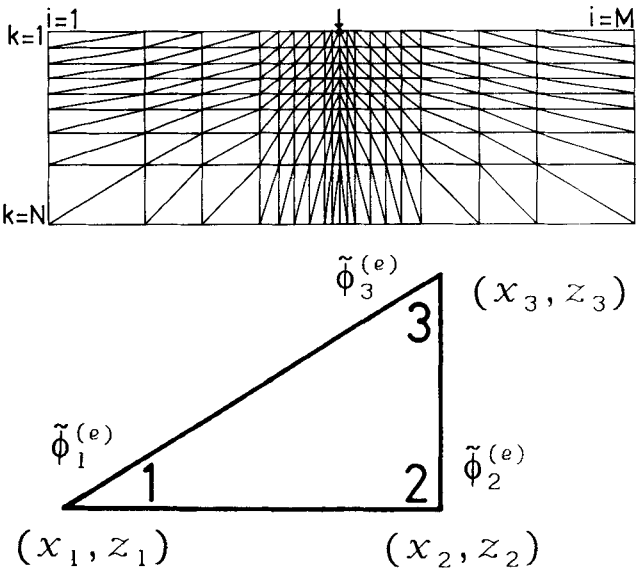

FIG. 1. MMR finite-element modeling, (a) finite-element mesh and (b) triangular element.

The final equation can be obtained by the combination of all element equations. Then the electric potential distribution inside the earth can be solved.

The computation of magnetic field intensity

Once the electric potential distribution is known and the Bessel function value at any node in an element is assumed to be constant, the three components of the magnetic field generated at the ground surface are

$$B_x(x, \lambda, z) = \sum_m \frac{\mu K_0(\lambda\sqrt{(x - x'_m)^2 + (z - z'_m)^2})}{12\pi} \times n_z L_i[3\sigma_{air}(\tilde{\phi}_i^{(e)} + \tilde{\phi}_j^{(e)}) - \sigma_j^{(e)}(\tilde{\phi}_i^{(e)} + 2\tilde{\phi}_j^{(e)}) - \sigma_i^{(e)}(2\tilde{\phi}_i^{(e)} + \tilde{\phi}_j^{(e)})],$$

$$B_y(x, \lambda, z) = \sum_m \frac{\mu K_0(\lambda\sqrt{(x - x'_m)^2 + (z - z'_m)^2})}{12\pi A_m} \times [n_x(\tilde{\phi}_i^{(e)} c_i + \tilde{\phi}_j^{(e)} c_j) - n_z(\tilde{\phi}_i^{(e)} b_i + \tilde{\phi}_j^{(e)} b_j)]$$

$$\times [3\sigma_{\text{air}}(\tilde{\phi}_i^{(e)} + \tilde{\phi}_j^{(e)}) - \sigma_j^{(e)}(\tilde{\phi}_i^{(e)} + 2\tilde{\phi}_j^{(e)}) - \sigma_i^{(e)}(2\tilde{\phi}_i^{(e)} + \tilde{\phi}_j^{(e)})],$$

$$B_z(x, \lambda, z) = \sum_m \frac{-\mu K_0(\lambda\sqrt{(x - x'_m)^2 + (z - z'_m)^2})}{6\pi} \times n_x L_i[3\sigma_{air}(\tilde{\phi}_i^{(e)} + \tilde{\phi}_j^{(e)}) - \sigma_j^{(e)}(\tilde{\phi}_i^{(e)} + 2\tilde{\phi}_j^{(e)}) - \sigma_i^{(e)}(2\tilde{\phi}_i^{(e)} + \tilde{\phi}_j^{(e)})], \tag{12}$$

where (x'_m, z'_m) are the coordinates of the geometric center of element m, n_x and n_z are direction cosines of the outward normal unit vector on the ground surface in the x- and z- directions, respectively, and σ_{air} is the conductivity of the air.

VERIFICATION OF NUMERICAL RESULTS

Based on equation (12), the magnetic field in the x-λ-z domain can be calculated by using variational calculus and Cholesky decomposition. To inspect the reliability of our algorithms, we compare the numerical values with analytic

ones for the electric potential and apparent resistivity for well-known geoelectric models. A total of 124 points from 0 to 3.05 in the wavenumber domain are selected for calculating the magnetic field $\mathbf{B}(x, \lambda, z)$. Then the components of magnetic field $\mathbf{B}(x, y, z)$ are computed based on equation (5) through a cubic spline interpolation from $\mathbf{B}(x, \lambda, z)$. More precise numerical results can be obtained through this procedure. Figure 2 shows the analytic and numerical results for a half-space model with a resistivity of 100 $\Omega \cdot$ m. The numerical errors for both electric potential and apparent resistivity are less than 6 percent. Figure 3 shows the results for a two-layer model. The top layer with a resistivity of 10 $\Omega \cdot$ m has a thickness of 4 units, and the resistivity of the lower half-space is 100 $\Omega \cdot$ m. The maximum error for the x- and z-component of the magnetic field can be evaluated at the point on the vertical contact of a normal fault model in which the resistivity on the left-hand side is 100 $\Omega \cdot$ m and 10 $\Omega \cdot$ m on the right-hand side. (Figure 4a). Figure 4a also shows that at point $(x, 0, 0)$, where the half distance between current electrodes equals 14 units, the numerical values of the x- and z-component (denoted by circles and

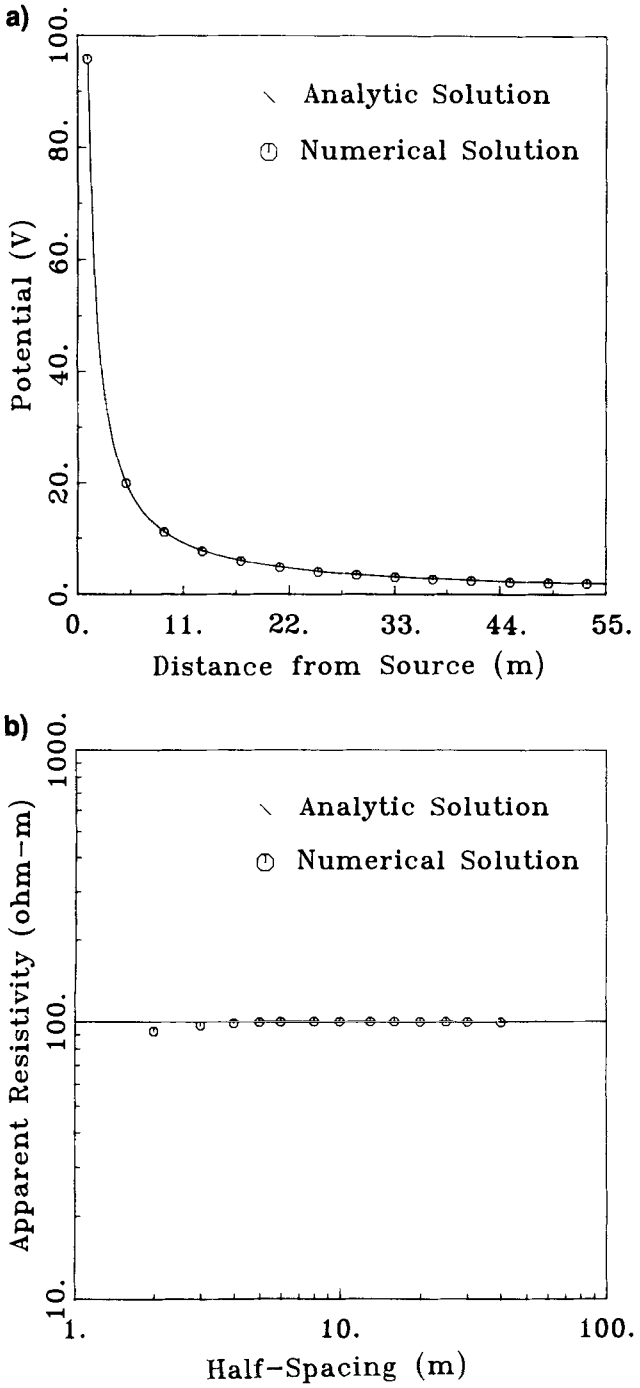

FIG. 2. Analytic and numerical solutions for a half-space model, (a) for electric potential and (b) for apparent resistivity.

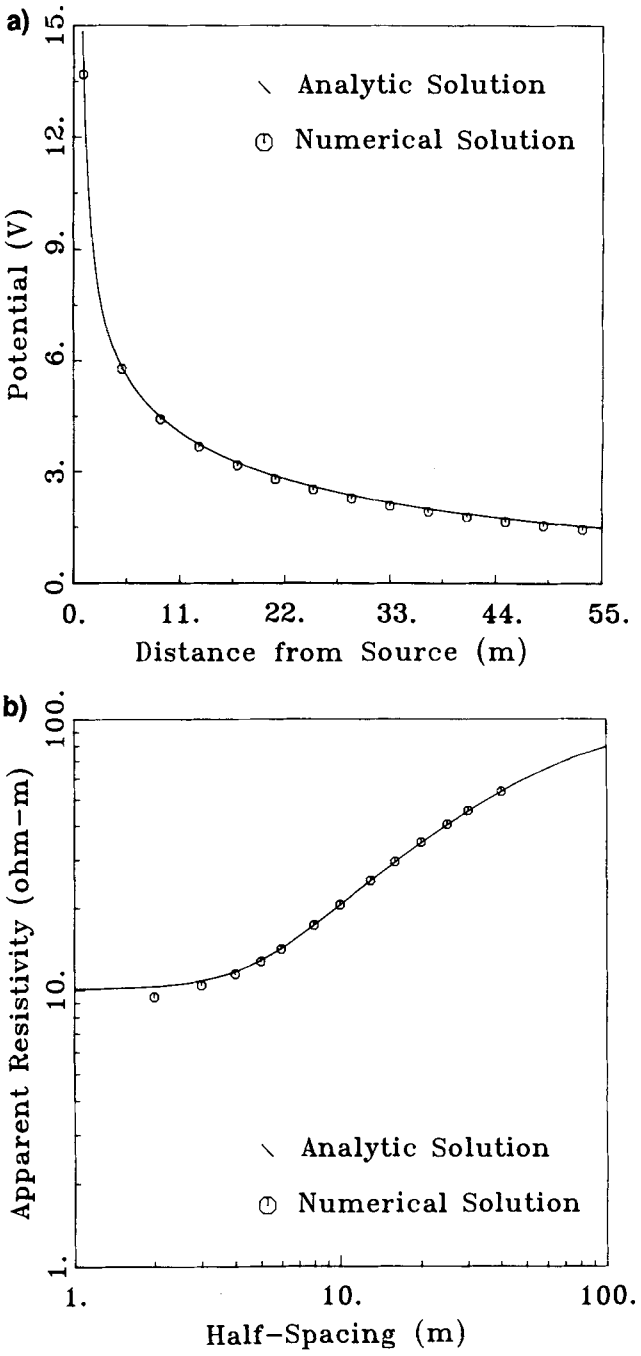

FIG. 3. Analytic and numerical solutions for a two-layer model, (a) for electric potential and (b) for apparent resistivity.

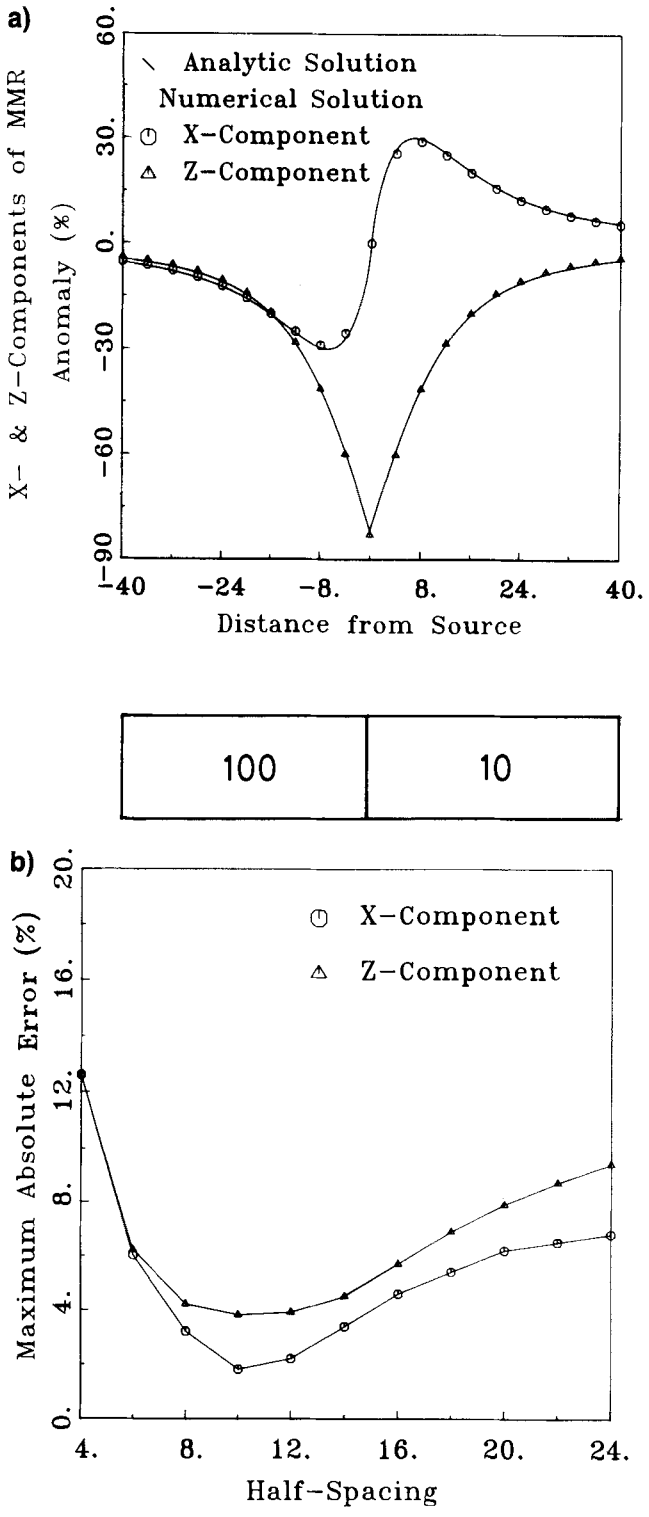

FIG. 4. (a) Vertical contact fault model, analytic, and numerical solutions of the x- and z-component of the MMR responses. (b) The maximum error as a function of half the distance between the two current electrodes.

triangles, respectively) of the MMR anomalies are very close to the analytic solutions (represented by solid lines). Figure 4b gives the dependence of the maximum error upon half spacing, half the distance between current electrodes. The values less than 5 percent appear at 8, 10, 12, and 14 units.

MODELING RESULTS

Topographic relief should be a significant factor affecting the current flow pattern. To study topographic effects, we use the MMR anomaly for each component of the magnetic field at location $(x, 0, z)$ as defined by Edwards et al. (1978):

$$\text{MMR anomaly}(\%) = \frac{B_i(x, 0, z) - B_i^n(x, 0, 0)}{B_i^n(0, 0, 0)} \times 100\% \tag{13}$$

in which $B_i(x, 0, z)$ is the computed value (or observed value) of the magnetic field, $B_i^n(x, 0, 0)$ is the theoretical value for a flat half-space, and $B_i^n(0, 0, 0)$ is the theoretical value at the center of the profile, i.e., $x = 0$. Topographic effects for three models: a trapezoidal hill, a trapezoidal valley, and a ramp are studied.

Trapezoidal hill model

Figure 5a shows a trapezoidal hill with a width of 14 units. Three different heights of 2, 3, and 4 units are considered. The resistivity is homogeneous. The MMR topographic anomalies are calculated on the surface. Current electrodes 28 units apart are positioned at the middle point of the hill parallel to the model strike-direction. The measurement profile is centered between and perpendicular to the current electrodes. Figure 5b is the profile of the x-component (perpendicular to strike) anomalies for different elevations versus the surveying location. The circles, triangles and crosses represent the topographic anomalies for three elevations: 2, 3, and 4 units, respectively. Results show that the most anomalous values appear at the hill region. The effect decreases rapidly downhill and finally approaches zero, as the receiver is far away from the hill. The cusps present on the figure may be caused by the disturbance of the current flow at the sharp corners of the raised region of the hill models. The Figure also indicates that a higher hill has a larger topographic anomaly. Figure 5c is the profile of the z-component anomalies. An antisymmetric type of anomaly can be recognized. A nodal point (zero anomaly) is located at the middle of the hill between the two current electrodes. Similar to the case for the x-component anomalies, the z-component terrain effect also increases with the elevation of the hill. The extreme value of the anomalies is around the lower break of the slope of the hill. The terrain effect also decreases rapidly with the distance from the foot of the hill. Figure 5d is the plot of the x-component of MMR anomalies for the hill models with fixed height but different widths. The MMR topographic anomalies decrease with width. The same results also occur for the z-component anomalies (see Figure 5e).

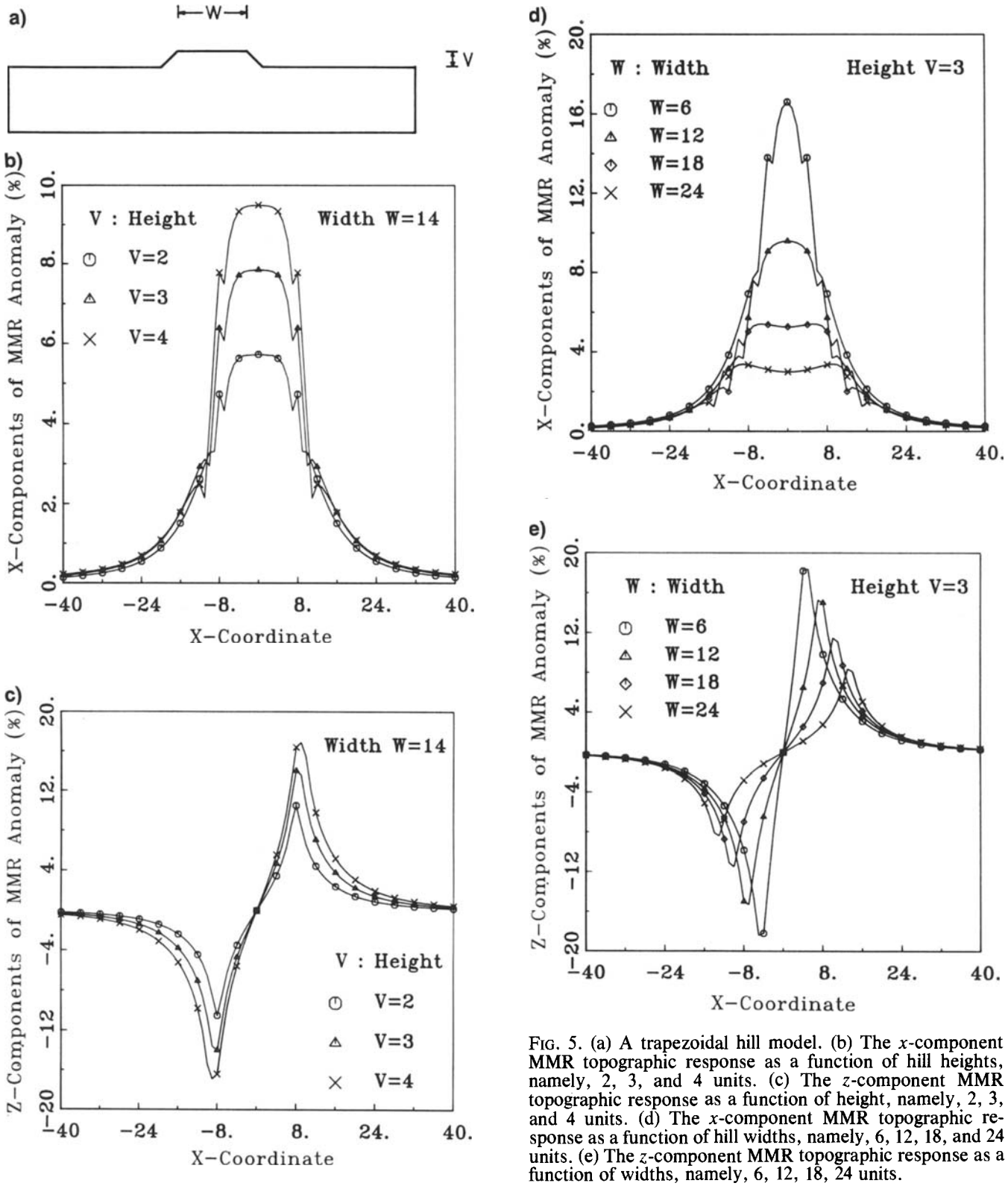

FIG. 5. (a) A trapezoidal hill model. (b) The x-component MMR topographic response as a function of hill heights, namely, 2, 3, and 4 units. (c) The z-component MMR topographic response as a function of height, namely, 2, 3, and 4 units. (d) The x-component MMR topographic response as a function of hill widths, namely, 6, 12, 18, and 24 units. (e) The z-component MMR topographic response as a function of widths, namely, 6, 12, 18, 24 units.

Trapezoidal valley model

Figure 6a shows a trapezoidal valley model with a uniform resistivity. The depths of the valley base vary from 2 to 4 units. The width of the valley base is 24 units. The symbols shown in Figure 6b are the same as those used in Figure 5b. The behavior of the x-component anomalies at the flat base is very similar to those shown on the raised flat region of the hill model, except for a different sign. The anomalies outside the valley have the same trend as those apart from the raised flat region shown on the hill model. For the former (Figure 5b) the anomaly markedly decreases from the upper break of the slope; while for the latter (Figure 6b) the anomaly increases from the lower break of the slope to the upper break of the slope, and then decrease again. The z-component anomalies (Figure 6c) have the same characteristic as those for the hill model (Figure 5c), except for the polarity of the anomalies. Figures 6b and 6e show the variations of the x-component or z-component MMR anomalies with the width of the valley. It is obvious that the topographic anomalies reduce as the width of the valley increases.

Ramp models

The ramp model is shown in Figure 7a. In the Figure, A is the angle of the slope and H is the height of the raised portion. The earth resistivity is homogeneous. The effect of topographic relief on the MMR measurements is studied for models with a height of 4 units and different dips of 18, 28, 45, 64, 72, and 90 degrees. The current source is positioned on the upper break of the slope. For the x-component anomalies as shown in Figure 7b, the computed curves are antisymmetric. In general, the upper break of the slope has larger anomalies than the lower break of the slope. The amplitude of the anomaly increases as the dip angle and distance increase. The z-component of the anomaly is shown on Figure 7c. The values of the anomaly are positive, and the peak value is near the upper break of the slope. The steeper the slope, the larger the anomaly. Figure 7d and 7e show the anomalies caused by a steep cliff model, i.e., $A = 90$ degrees. An antisymmetric x-component anomaly (Figure 7d) and peak anomaly values at the vertical boundary for the z-component anomalies (Figure 7e) can be recognized. The magnitude of the anomalies increase as the height of the raised portion increases.

TOPOGRAPHIC CORRECTION

Oppliger (1984) has suggested that the topographic correction for the MMR method can be made as follows:

corrected MMR anomaly
= observed values − computed values due to a homogeneous half-space with terrain.

This formulation has been used to demonstrate a 45-degree dipping fault model incorporating a 45-degree ramp surface. The fault zone has a resistivity of 10 $\Omega \cdot$ m, and the host has a resistivity of 100 $\Omega \cdot$ m (Figure 8a). The same fault model with a flat surface is shown in Figure 8b. The computed x-component and z-component of the MMR anomalies with terrain effect (circle), without terrain effect (triangle) and the anomalies after topographic correction (cross) are shown in Figure 8c and 8d, respectively. The results having the topographic correction match well with the results for the same fault model with no topographic anomaly.

CONCLUSIONS

In this paper, the finite-element technique has been applied to develop algorithms to study the terrain effects on the MMR responses for 2-D topographic models. In the modeling process, a nonhomogeneous element instead of a homogeneous element has been used to handle the interface of differing conductivity and geoelectric structure with linearly varying conductivity. We have illustrated the MMR topographic anomalies for trapezoidal hill, trapezoidal valley, and ramp models. These results provide us with a quantitative topographic correction for the MMR sounding data. The results of this study agree in general with those of Oppliger (1984) and show that (1) the terrain effects could affect the sounding interpretation in a manner similar to buried lateral inhomogeneities and to obtain a better subsurface picture, we have to remove these effects on the MMR sounding data, (2) the more rugged the ground surface, the larger the MMR topographic anomaly, (3) the terrain effects do depend on the source and/or receiver positions and in general, the anomalies will be decreased as the distance between the source position (or/and receiver position) and the relief area is increased, (4) the characteristic of the anomaly curves does depend on the form of the topography, and (5) the numerical example indicates the finite-element modeling technique does provide a means of determining topographic correction for MMR sounding data over 2-D topography.

ACKNOWLEDGMENTS

The author is indebted to the National Science Council, Republic of China, for financial support under Grant NSC75-0202-M008-08.

REFERENCES

Coggon, J. H., 1971, Electromagnetic and electrical modeling by the finite element method: Geophysics, **36**, 132–155.
Dey, A., and Morrison, H. F., 1979, Resistivity modeling for arbitrarily shaped two-dimensional structures: Geophys. Prosp., **27**, 106–136.
Edwards, R. N., Lee, H., and Nabighian, M. N., 1978, On the theory of magnetometric resistivity (MMR) methods: Geophysics, **43**, 1176–1203.
Fox, R. C., Hohmann, G. W., Killpack, T. J., and Rijo, L., 1980, Topographic effects in resistivity and induced polarization surveys: Geophysics, **45**, 75–93.
Holcombe, H. T., and Jiracek, G. R., 1984, Three dimensional terrain corrections in resistivity surveys: Geophysics, **49**, 439–452.
Oppliger, G. L., 1984, Three-dimensional terrain corrections for mise-a-la-masse and magnetometric resistivity surveys: Geophysics, **49**, 1718–1729.
Pai, D., and Edwards, R. N., 1983, Finite-difference modeling of MMR anomalies: Research in applied geophysics, No. 25, Univ. of Toronto, Dept. of Geophysics.
Tseng, C. L., Yang, C. H., and Liao, C. S., 1985, MMR Modeling study by finite-difference method: Proceedings of the National Science Council, **9**, 121–162, NSC, Rep. of China.

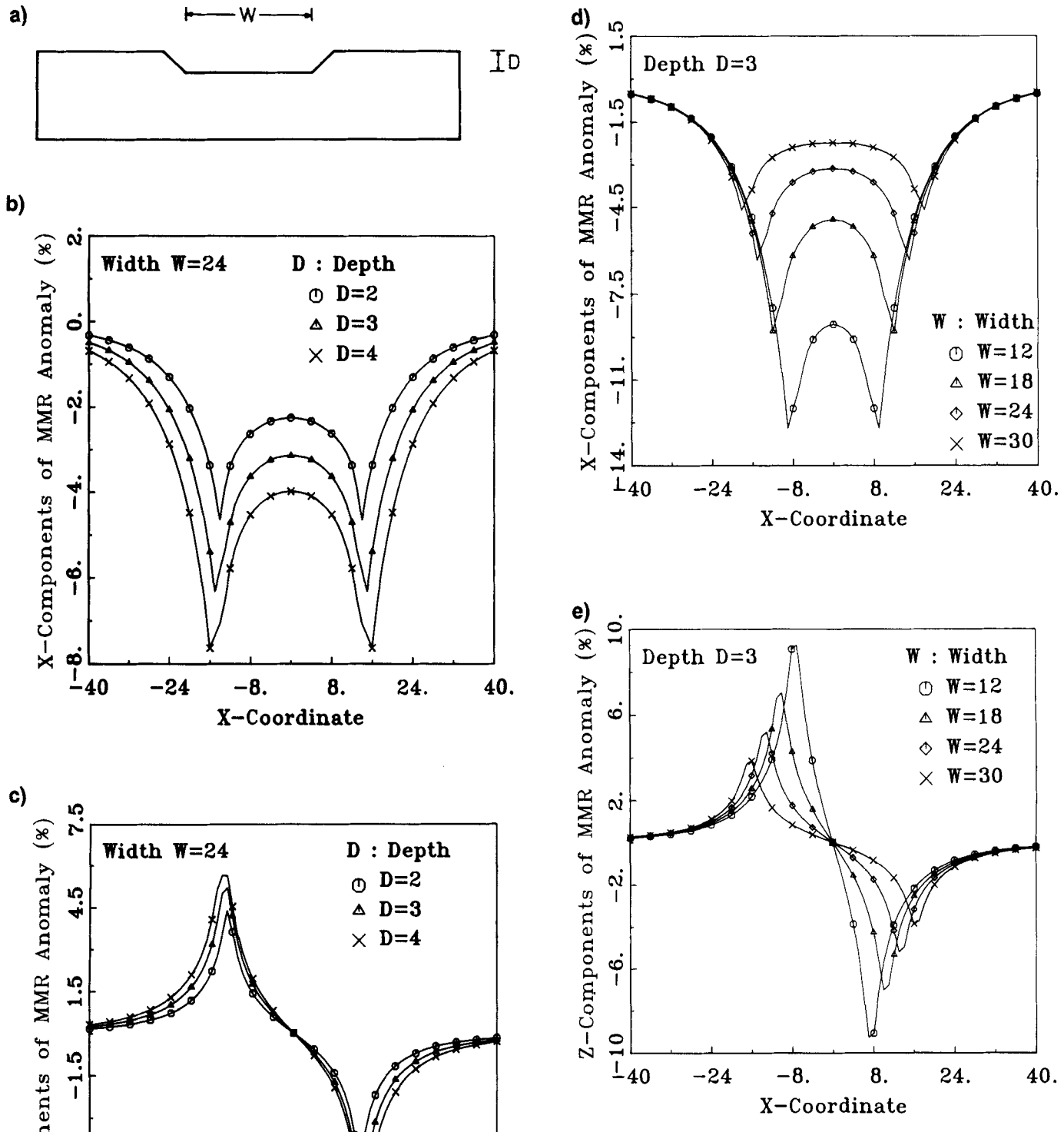

FIG. 6. (a) A trapezoidal valley model. (b) The x-component MMR topographic response as a function of depression depth, namely, 2, 3, and 4 units. (c) The z-component topographic response as a function of depression depth, namely, 2, 3, and 4 units. (d) The x-component MMR topographic response as a function of anomaly width, namely, 12, 18, 24, and 30 units. (e) The z-component MMR topographic response as a function of anomaly width, namely, 12, 18, 24, and 30 units.

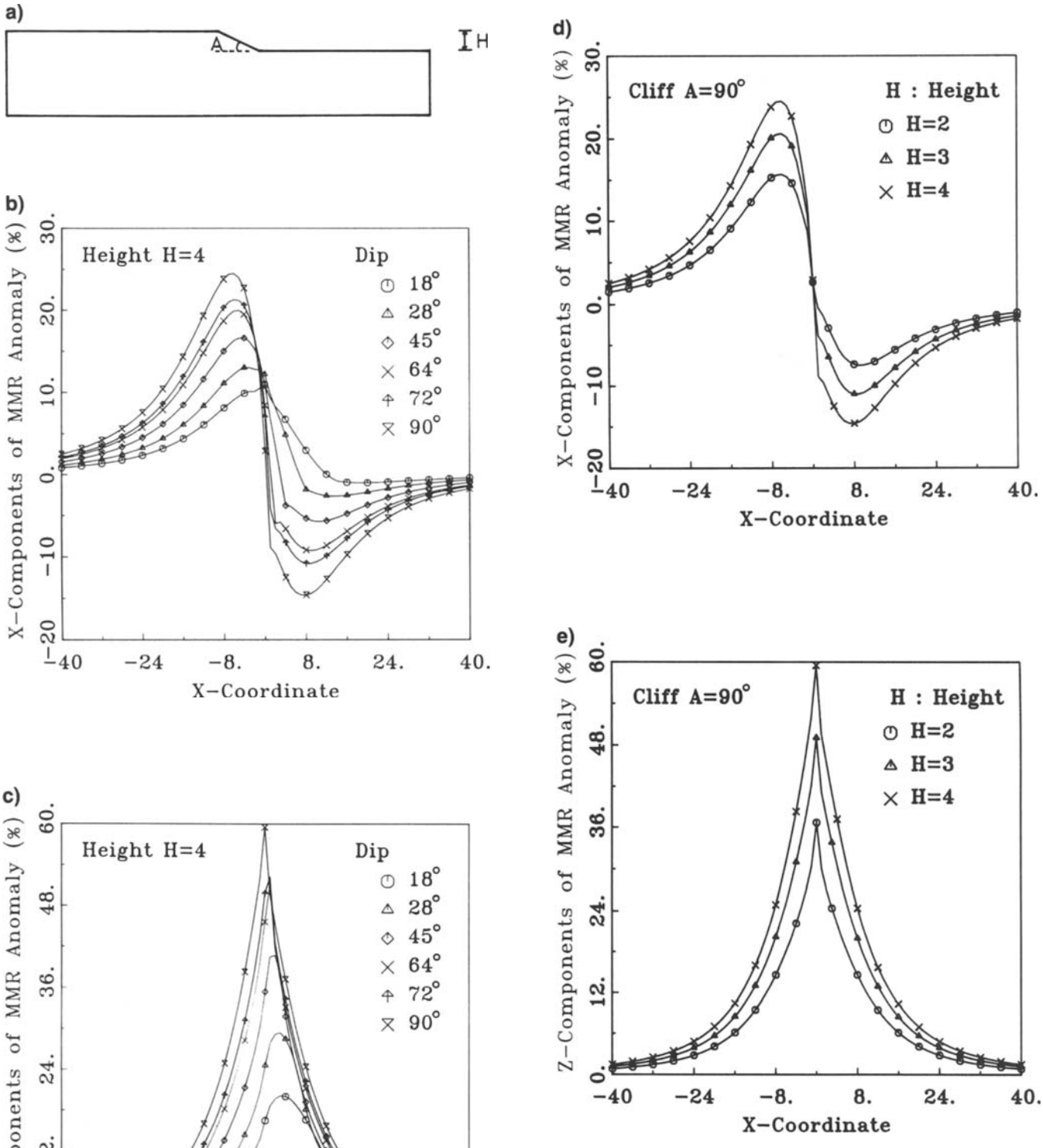

FIG. 7. (a) A ramp model. (b) The x-component MMR topographic response as a function of dip, namely, 18, 28, 45, 64, 72, and 90 degrees. (c) The z-component MMR topographic response as a function of dip, namely, 18, 28, 45, 64, 72, and 90 degrees. (d) The x-component MMR topographic response as a function of height, namely, 2, 3, and 4 units. (e) The z-component MMR topographic response as a function of height, namely, 2, 3, and 4 units.

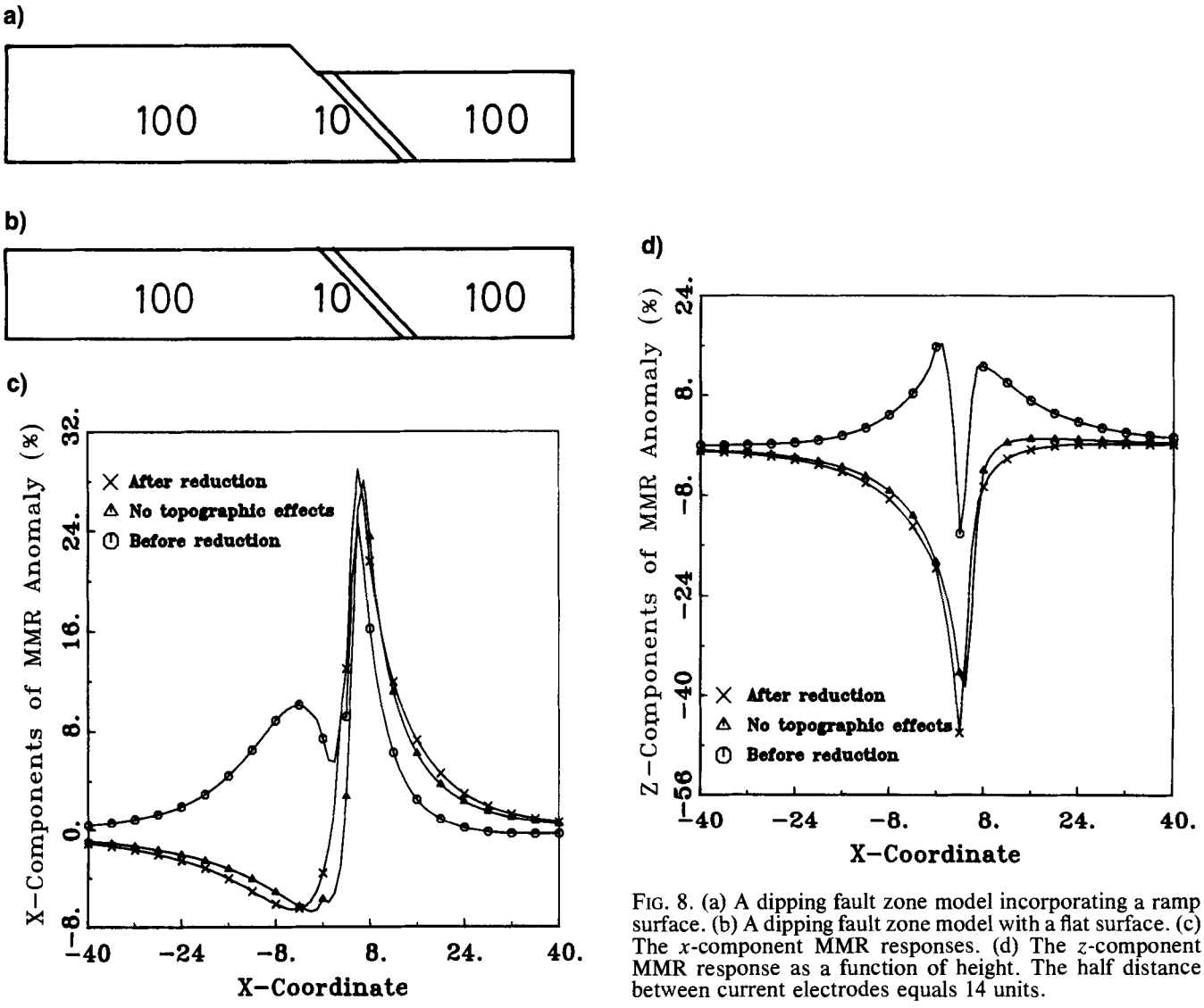

FIG. 8. (a) A dipping fault zone model incorporating a ramp surface. (b) A dipping fault zone model with a flat surface. (c) The x-component MMR responses. (d) The z-component MMR response as a function of height. The half distance between current electrodes equals 14 units.